Application of an Equiaxed Grain Growth and Transport Model to Study Macrosegregation in a DC Casting Experiment

AKASH PAKANATI, KNUT OMDAL TVEITO, MOHAMMED M'HAMDI, HERVÉ COMBEAU, and MIHA ZALOŽNIK

A simplified three-phase, multiscale macrosegregation model which describes the growth kinetics of equiaxed grains and the coupling between microstructure morphology and the macroscopic transport has been proposed previously. In this paper, the model is validated by comparing the numerical model predictions to the experimental data from DC casting of an AA7050 alloy billet. The morphology of the equiaxed grains has an important influence on the macrosegregation, and we show that the model predictions are accurate when the grain morphology is described correctly.

I. INTRODUCTION

ONE of the main phenomena causing macrosegregation in direct-chill (DC) cast aluminium alloy products is the motion of free-floating equiaxed grains. The solute-lean grains settle toward the bottom of the solidification zone (mushy zone) and eject solute-rich liquid. This tends to cause negative macrosegregation in the vicinity of the centerline of the casting, and positive macrosegregation elsewhere. The intensity of this effect on macrosegregation depends largely on the morphology of the equiaxed grains—dendritic or globular.[1–4] The grain morphology has an impact on the motion and the packing of free-floating equiaxed grains[5] as well as on the permeability of the packed grain layer. The development of the microstructure (grain size, morphology) is also strongly conditioned by macroscopic flow, which determines the transport of grains and of inoculant particles that act as nucleation sites, throughout the casting.[6]

Control of microstructure and of macrosegregation in DC casting *via* various process parameters, such as casting speed, grain refinement or melt feeding, require a detailed understanding of the involved physical mechanisms. Such understanding is still lacking and the support of modeling is vital to improve the control of the complex casting process. Volume-average multiscale and multiphase models that couple the description of the process-scale transport with detailed models of dendritic grain growth have been developed for around 30 years[3,7–13] and have been applied to other casting processes, mainly to steel ingot castings.[14–17] This type of modeling is much less developed for DC casting of aluminum alloys. Most DC casting models were based on simple solidification models and did not account for the description of nucleation and of grain growth kinetics.[18–23] Models that included grain growth kinetics did either not consider grain motion at all[1] or assumed a globular morphology for the free-floating grains.[23,24] Detailed models that focused on grain structure and morphology were not coupled with grain motion and macrosegregation.[25] Simulations of macrosegregation were thus limited to globular grains and could not correctly describe the influence of grain morphology.

Only recently a multiscale model of DC casting, sufficiently advanced to describe the morphology development during grain growth, fully coupled with grain motion, and macrosegregation, was developed and applied by Tveito *et al.*[3] This three-phase volume-averaged[8] model accounts for solidification shrinkage, thermosolutal convection, grain transport, heat transfer, solute transport, and equiaxed grain growth. In addition to these aspects, nucleation on grain refiners and strong coupling between nucleation, growth, and transport of grain refiner particles, which are important in DC casting of Al alloys, are also accounted for in this model.

AKASH PAKANATI and KNUT OMDAL TVEITO are with the Department of Materials Technology, NTNU, 7491 Trondheim, Norway. MOHAMMED M'HAMDI is with the Department of Materials Technology, NTNU and also with the SINTEF Materials and Chemistry, 0314 Oslo, Norway. Contact e-mail: Mohammed.Mhamdi@sintef.no HERVÉ COMBEAU and MIHA ZALOŽNIK are with the Université de Lorraine, CNRS Institut Jean Lamour – IJL, 54000, Nancy, France.
Manuscript submitted July 9, 2018.
Article published online February 13, 2019.

The impact of grain morphology on macrosegregation formation in a DC-cast ingot was shown qualitatively. This model was also successfully applied to analyze the influences of the flow and of grain refinement on grain size and morphology in a large sheet ingot[26,27] and in a cylindrical billet.[4]

In this paper, we use the model of Tveito et al. to investigate the influence of melt feeding on the formation of macrosegregation and microstructure in DC-cast AA7050 alloy billets. The study is based on experiments conducted by Zhang et al.[21,28] We show that the description of grain morphology is an essential model ingredient for an accurate prediction of macrosegregation formation.

II. NUMERICAL MODEL

The three-phase, multiscale numerical model of equiaxed solidification proposed by Tveito et al.,[3] is based on the volume-averaging approach of Wang and Beckermann[9] and employs the operator-splitting algorithm proposed by Založnik and Combeau.[13] For a detailed description of the model, the reader is referred to these references. Only the main features are described here, and the model equations are summarized in Table I. The Euler–Euler volume-averaged model has two parts—macroscopic transport and microscopic growth. The macroscopic transport model accounts for solute and heat transfers coupled with liquid flow induced by solidification shrinkage and thermosolutal convection. The densities of liquid and solid are assumed to be constant but different, and the Bousinessq approximation is used for the liquid density, accounting for thermal and solutal effects in the buoyancy term. The volume occupied by a dendritic grain is given by the volume of its envelope. Two flow regimes are considered, and the flow regime depends on the local volume fraction of the grain envelopes (g_{env}). For envelope fractions smaller than the packing fraction (g_{pack}, a model parameter) the solid (equiaxed) grains are freely floating. The interfacial drag coefficient, C_D, in Eq. [9] is modeled in the same manner as described in Reference 13 for spherical particles, but by considering the envelope fraction instead of the solid fraction. For envelope fractions greater than the packing fraction, the equiaxed grains are assumed to form a rigid porous solid matrix moving with the casting velocity, $\vec{V}_{cast}$. The interfacial drag in the porous medium is modeled by a Darcy term, where the hydrodynamic permeability is calculated by the Kozeny Carman relation, using a characteristic length scale of the porous microstructure, l_{KC}.

The microscopic model part is treated locally within each volume element. In the model of grain growth kinetics, finite diffusion in both solid and liquid phases is accounted for, and local thermal equilibrium is assumed. Nucleation of grains is assumed to occur on grain-refiner (inoculant) particles. According to the athermal nucleation theory of Greer et al.[29] the critical undercooling for free growth of a grain on an inoculant particle of diameter d is given by $\Delta T_c = 4\Gamma_{GT}/d$, where Γ_{GT} is the Gibbs–Thompson coefficient. The number of activated inoculant particles then depends on the size distribution of the particle population, which can be represented by an exponential distribution density function This representation holds for the largest particles, which are activated at small undercoolings and, therefore successful as nuclei. This size distribution is then discretized into m classes of inoculants. Each class i is represented by a number density, N_{nuc}^i, and a critical undercooling, ΔT_c^i. When the local undercooling reaches the critical undercooling of class i, its local inoculant number density, N_{nuc}^i, is instantaneously added to the grain number density, N_g, and N_{nuc}^i becomes locally zero. The conservation equations for the number density of each inoculant class and the grain number density are shown in Eqs. [10] and [11], respectively, where Φ^i represents the transfer of number density from inoculants to grains upon nucleation.

The diffusion-controlled growth of dendritic grains is described by a volume-averaged model that distinguishes three hydrodynamic phases: solid (g_s), intragranular liquid (g_d), and extragranular liquid (g_e).[30] The sum of the volume fraction of the three phases is unity ($g_s + g_d + g_e = 1$). The distinction between the two liquid phases is made because the diffusion time in the intragranular liquid is governed by the secondary dendrite arm spacing (SDAS) and in the extragranular liquid by the distance between grains. The intragranular liquid is at the thermodynamic equilibrium throughout the solidification because of the short diffusion time at the SDAS scale. The extragranular liquid remains undercooled, and the undercooling depends on the solute diffusion from the intragranular liquid into the extragranular liquid. The growth of the solid is governed by diffusion at the solid–intragranular liquid interface. The grain envelopes are assumed to be spheres growing with the speed of the primary dendrite tips. Their growth is given by a model of a hemispherical dendrite tip, which links the tip speed to the volume-averaged undercooling in the extragranular liquid. Since it distinguishes between the growth of the solid skeleton and that of the grain envelope, the model gives a quantitation of the grain morphology via the fraction of solid in the envelope—the internal solid fraction: $g_{intern} = g_s/g_{env}$. For $g_{intern} \ll 1$, the grains are considered to be dendritic; for $g_{intern} \approx 1$, they are globular.

The grain growth in the microscopic model is described by a representation based on three hydrodynamic phases. However, the macroscopic transport model is formulated in terms of two phases: the solid and the liquid phases. This simplification follows from the assumption of equal velocities of the intragranular and extragranular liquid phases and of the combination of the solutal conservation equations for the two liquid phases. This approach, described in Reference 3, results in a single liquid-phase solute transport equation, leading to a two-phase formulation of the macroscopic transport model.

Table I. System of Equations

Macroscopic Conservation Equations

Averaged mass balance of liquid phase

[1] $$\frac{\partial}{\partial t}(\rho_l g_l) + \nabla \cdot (\rho_l g_l \langle \vec{v}_l \rangle^l) = \Gamma^l$$

Averaged mass balance of solid phase

[2] $$\frac{\partial}{\partial t}(\rho_s g_s) + \nabla \cdot (\rho_s g_s \langle \vec{v}_s \rangle^s) = \Gamma^s$$

Averaged solute balance of liquid phase for component i

[3] $$\frac{\partial}{\partial t}(\rho_l g_l \langle C_{i,l} \rangle^l) + \nabla \cdot (\rho_l g_l \langle \vec{v}_l \rangle^l \langle C_{i,l} \rangle^l) = -\Gamma^s C_i^{*,l} + \frac{\rho_l S_v^{env} D_{i,l}}{\delta_i^{c-d}} \frac{g_l}{g_e}\left(C_i^{*,l} - \langle C_{i,l} \rangle^l\right)$$

Averaged solute balance of solid phase for component i

[4] $$\frac{\partial}{\partial t}(\rho_s g_s \langle C_{i,s} \rangle^s) + \nabla \cdot (\rho_s g_s \langle \vec{v}_s \rangle^s \langle C_{i,s} \rangle^s) = \Gamma^s C_i^{*,s-d} + \frac{\rho_s S_v^s D_{i,s}}{\delta_i^{s-d}}\left(C_i^{*,s-d} - \langle C_{i,s} \rangle^s\right)$$

Averaged mixture enthalpy

Averaged envelope fraction

[5] $$\frac{\partial}{\partial t}(\rho_m h_m) + \nabla \cdot (\rho_s g_s \langle \vec{v}_s \rangle^s \langle h_s \rangle^s) + \nabla \cdot (\rho_l g_l \langle \vec{v}_l \rangle^l \langle h_l \rangle^l) = \nabla \cdot ((g_l \kappa_l + g_s \kappa_s)\nabla T)$$

[6] $$\frac{\partial}{\partial t}(\rho_s g_{env}) + \nabla \cdot (\rho_s g_{env} \langle \vec{v}_s \rangle^s) = \Gamma^{env}$$

Averaged liquid momentum

[7] $$\frac{\partial}{\partial t}(\rho_l g_l \langle \vec{v}_l \rangle^l) + \nabla \cdot (\rho_l g_l \langle \vec{v}_l \rangle^l \langle \vec{v}_l \rangle^l) = -g_l \nabla p_l + \nabla \cdot (g_l \mu_l \nabla \langle \vec{v}_l \rangle^l) + g_l \rho_l^b \vec{g} + M_{ls}$$

Averaged solid momentum

[8] $$0 = -g_s \nabla p_l + g_s \rho_s^b \vec{g} - M_{ls} \qquad g_{env} < g_{pack}$$
$$\langle \vec{v}_s \rangle^s = \vec{V}_{cast} \qquad g_{env} > g_{pack}$$

Source term in momentum equation

[9] $$M_{ls} = \begin{cases} \frac{3 g_{env} C_D |\vec{v}_r| Re}{4(2R_{env})^2 (1-g_{env})}\left(\langle \vec{v}_s \rangle^s - \langle \vec{v}_l \rangle^l\right) & g_{env} < g_{pack} \\ \frac{g_l^2 \mu_l}{K}\left(\langle \vec{v}_s \rangle^s - \langle \vec{v}_l \rangle^l\right), \quad K = \frac{\lambda_c}{180}\frac{g_l^3}{(1-g_l)^2} & g_{env} > g_{pack} \end{cases}$$

Nucleation Modeling

Innoculant Motion

[10] $$\frac{\partial}{\partial t}(N_{nuc}^i) + \nabla \cdot (\langle \vec{v}_l \rangle^l N_{nuc}^i) = -\Phi^i$$

Grain Population Balance

[11] $$\frac{\partial}{\partial t}(N_g) + \nabla \cdot (\langle \vec{v}_s \rangle^s N_g) = \sum_{i=1}^{N_{nuc}^i} \Phi^i$$

Source Term in Nucleation Modeling

[12] $$\Phi^i = \begin{cases} N_{nuc}^i \partial(t), \Delta T < \Delta T_c^i, & i = 1,\ldots,m \\ 0, & \text{else} \end{cases}$$

Microscopic Conservation Equations

Mass Balance at Solid–Liquid Interface

[13] $$\Gamma_l + \Gamma_s = 0$$

Solute Balance at Solid–Liquid Interface

[14] $$\Gamma^s(1-k_{p,i})C_i^{*,l} = \frac{\rho_s S_v D_{i,s}}{\delta_i^{s-d}}\left(k_{p,i} C_i^{*,l} - \langle C_{i,s} \rangle^s\right) + \frac{\rho_l S_v^{env} D_{i,l}}{\delta_i^{c-d}}\frac{g_l}{g_e}\left(C_i^{*,l} - \langle C_{i,l} \rangle^l\right)$$

Growth Rate of Grain Envelope. The Tip Velocity (V_{tip}) is Computed Using Hemispherical Tip Model Proposed by Rappaz and Boettinger[31]

[15] $$\Gamma^{env} = \rho_l S_v^{env} V_{tip}$$

Diffusion Lengths

[16] $$\delta_i^{s-d} = \frac{R^{s,eq}}{5}$$

Table I.   continued

$$\delta_i^{\mathrm{e-d}} = d_i \left\{ \frac{d_i}{R^{\mathrm{env}}} - \omega \right\}^{-1}$$

[17]

$$\omega = \frac{f(R^{\mathrm{env}}, \Delta_i) + g(R_f, R^{\mathrm{env}}, \Delta_i)}{d_i[R^{\mathrm{env}} + d_i - (R^{\mathrm{env}} + \Delta_i + d_i)e^{-\Delta_i/d_i}] - f(R^{\mathrm{env}}, \Delta_i) + (e^{-\Delta_i/d_i} - 1)g(R_f, R^{\mathrm{env}}, \Delta_i)}$$

$$R_f = \left(\frac{3}{4\pi N_g} \right)^{1/3}, \quad R^{\mathrm{env}} = R_f g_{\mathrm{env}}^{1/3}, \quad R^{\mathrm{s,eq}} = R_f g_s^{1/3}, \quad S_v^{\mathrm{env}} = 4\pi (R^{\mathrm{env}})^2 N_g, \quad S_v^s = 4\pi (R^{\mathrm{s,eq}})^2 N_g$$

$$d_i = D_{\mathrm{l},i}/V_{\mathrm{tip}}, \quad f(R_{\mathrm{env}}, \Delta_i) = \frac{[(R^{\mathrm{env}} + \Delta_i)^2 - (R^{\mathrm{env}})^2]}{2}$$

$$g(R_f, R^{\mathrm{env}}, \Delta_i) = \frac{\left[(R_f)^3 - (R^{\mathrm{env}} + \Delta_i)^3 \right]}{[3(R^{\mathrm{env}} + \Delta_i)]},$$

$$\Delta_i = \frac{2R^{\mathrm{env}}}{Sh_i}$$

$$Sh_i = \frac{2}{3(1 - g_{\mathrm{env}})} Sc_i^{1/3} \mathrm{Re}^{n(\mathrm{Re})},$$

$$n(\mathrm{Re}) = \frac{2\mathrm{Re}^{0.28} + 4.65}{3(\mathrm{Re}^{0.28} + 4.65)},$$

$$\mathrm{Re} = \frac{\rho_l(1 - g_{\mathrm{env}})(2R^{\mathrm{env}})}{\mu_l} \left| \langle \vec{v}_s \rangle^{\mathrm{s}} - \langle \vec{v}_l \rangle^l \right|$$

Thermodynamic relations at solid–liquid interface

$$C_i^{*,\mathrm{s-d}} = k_{\mathrm{p},i} C_i^{*,l}$$

$$Sc_i = \frac{\mu_l}{\rho_l D_{\mathrm{l},i}},$$

[18]

$$T_{\mathrm{liq}} = T_{\mathrm{m}} + \sum_i m_{l,i} c_{l,i}^*$$

[19]

$$\Delta T = T - T_{\mathrm{m}} - \sum_i m_{l,i} c_{l,i}^*$$

[20]

III. DC CASTING EXPERIMENT

The experiments are those performed by Zhang et al., and a detailed description of the experimental setup is found in References 21 and 28. Cylindrical AA7050 billets with a diameter of 315 mm were cast in a conventional DC casting mold without hot top. The casting temperature was 680 °C, and all the billets were grain refined by the same amount of Al5Ti1B master alloy, 2 kg/ton. Four billets were cast, each under different casting conditions. Two types of melt feeding schemes were used. The melt was poured into the mold either through a semi-horizontal feeding scheme or a vertical feeding scheme. In the former method, the melt was diverted to four branches through a cross-shaped splitter while in the latter method, the melt was poured directly in the center of the mold. Two casting speeds were used for each melt feeding scheme. For the semi-horizontal feeding scheme, speeds of 50 and 90 mm min^{-1} were used. For the vertical feeding scheme, speeds of 50 and 60 mm min^{-1} were used.

The alloy composition across the billet diameter was measured in points that were about 1 cm apart. The grain size was measured using the linear intercept method. The morphology of the grains was mostly dendritic. The grain size was observed to depend on the melt feeding scheme, which impacted the sump profile and the flow pattern in the liquid pool and slurry zone. The sump profile and the flow pattern were characterized by running 2D computer simulations using ALSIM6 (a casting simulation software developed by the Institute for Energy Technology, Kjeller, Norway). A low Rayleigh number (LRN) turbulent energy-pseudo turbulent dissipation ($k - \epsilon$) model was used to address the turbulence problem in the simulations.

IV. PROBLEM DESCRIPTION

The experiments are modeled as a 2D axisymmetric problem. The semi-horizontal melt feeding geometry (referred to as Inlet 1 from now on) is simplified by introducing a vertical inlet and a fixed disk 10 mm below the inlet, as shown in Figure 1. The vertical melt feeding geometry (referred to as Inlet 2 from now on) is obtained by removing the fixed disk from the geometry in Figure 1, resulting in the simplified geometry shown in Figure 2. In this paper, we analyze only the experiments with the casting velocity of 50 mm/min for both inlet schemes. Detailed boundary conditions for energy, liquid, and solid momentums are given in Table II. The inlet velocity is calculated from the global mass balance. The inlet temperature of the liquid metal is fixed at 953.15 K (680 °C), as in the experiments. The heat is extracted by primary cooling through the mold and by secondary cooling directly to the falling water film flowing over the ingot surface. Primary cooling consists of three zones: meniscus, mold, and air gap. The boundary conditions are specified in Table II with the ambient temperature (T_{amb}) specified for each boundary. The heat-transfer coefficient due to secondary
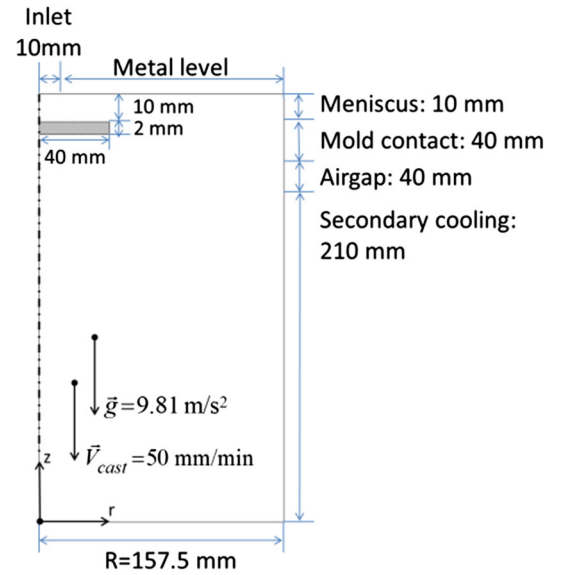

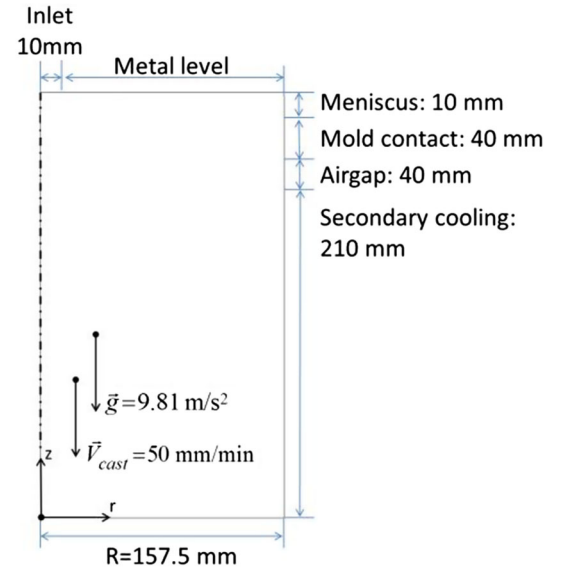Fig. 1—Simplified geometry of the semi-horizontal melt-feeding scheme (Inlet 1).

Fig. 2—Simplified geometry of the vertical melt-feeding scheme (Inlet 2).

cooling is modeled using the Weckmann and Niessen[32] correlation, given in Eq. [21].

$$
h_{\text{secondary}}(T) = \{A + B \cdot (T[\text{K}] + T_{\text{water}}[\text{K}])\}
$$
$$
\cdot \left(\frac{Q_{\text{water}}}{P}\right)^{1/3} + C \cdot \frac{(T - T_{\text{sat}})^3}{T - T_{\text{water}}},
$$
$$
A = -167000 \, [W \cdot s^{1/3} \cdot m^{-8/3}];
$$
$$
B = 352 \, [W \cdot s^{1/3} \cdot m^{-8/3} \cdot K^{-1}]; \quad C = 20.8 \, [W \cdot m^{-2} \cdot K^{-2}]
$$

[21]

where $h_{\text{secondary}}$ is the heat-transfer coefficient, T is the surface temperature of the ingot, T_{water} is the water

Table II. Boundary Conditions for Energy and Liquid Momentum

Boundary	Energy	Liquid Momentum
Inlet	$T_{cast} = 953.15$ K	calculated
Metal Level	$h_{primary} = 20$ W m^{-2} K^{-1}, $T_{amb} = 373.15$ K	slip
Meniscus	$h_{primary} = 0$ W m^{-2} K^{-1}	nonslip
Mold Contact	$h_{primary} = 600$ W m^{-2} K^{-1}, $T_{amb} = 293.15$ K	nonslip
Air Gap	$h_{primary} = 120$ W m^{-2} K^{-1}, $T_{amb} = 293.15$ K	nonslip
Direct Chill	based on Eq. [21]	nonslip
	$T_{amb} = T_{water} = 293.15$ K,	
	$T_{sat} = 373.15$ K,	
	$Q_{water} = 40$ l min^{-1}	
Outlet	—	—

Table III. Thermophysical Data for AA7050 Alloy Used in the Numerical Simulations

Property	Unit	Value	Property	Unit	Value
c_p	J kg^{-1} K^{-1}	1.3×10^3	ρ_l	kg m^{-3}	2468.7
L_f	J kg^{-1}	3.63×10^5	ρ_s	kg m^{-3}	2617.9
Γ_{GT}	K m	1.9×10^{-7}	$\rho_{s,b}$	kg m^{-3}	2538.9
μ_l	N S m^{-2}	1.28×10^{-3}	$\rho_{l,0}$	kg m^{-3}	2468.7
k_l	W m^{-1} K^{-1}	75.0	β_T	K^{-1}	-1.1×10^{-4}
k_s	W m^{-1} K^{-1}	185.0	l_{KC}	m	7.5×10^{-5}
T_m	K	940.15	g_{pack}	—	0.3
T_{eut}	K	723.15			

Property	Unit	Zn	Mg	Cu
$C_{0,i}$	wt pct	6.24	2.05	2.12
$k_{p,i}$	—	0.39	0.29	0.09
$m_{l,i}$	K wt pct^{-1}	-2.81	-3.88	-4.09
$D_{l,i}$	m^2 s^{-1}	$2.682 \times 10e^{-9}$	7.326×10^{-9}	4.372×10^{-9}
$D_{s,i}$	m^2 s^{-1}	$2.385 \times 10e^{-12}$	1.664×10^{-12}	8.363×10^{-13}
$\beta_{c,i}$	(wt pct)$^{-1}$	-1.23×10^{-2}	4.0×10^{-3}	-7.3×10^{-3}

temperature, T_{sat} is the boiling temperature of the water, Q_{water} is the water flow rate per ingot, and P is the ingot perimeter. All parameter values are given in Table II.

The thermophysical data for the AA7050 alloy are given in Table III. The linearized phase diagram defined by the liquidus slope, the partition coefficient, and the pure Al melting temperature, has been adjusted to fit the solidification path of AA7050, calculated with the microstructure code ALSTRUC.[33] The constant solute diffusion coefficients were calculated from Reference 34 at the liquidus temperature of the alloy at its nominal composition. The density of solid is assumed to be constant. The liquid density depends on the temperature and on the concentration of the alloy elements. The density evolution during solidification for both phases is shown in Figure 3(a), where the liquid density was calculated as function of solid fraction using a solidification path following the Scheil law. The grain packing fraction is a model parameter and its value is not known accurately. In DC casting modeling, packing fraction values between 0.15 and 0.3[4,23,24,35–37] are usually used. In the current study, the packing fraction is set to 0.3. Another poorly understood parameter value is the characteristic length (l_{KC}) used in the calculation of the permeability of the mushy zone. This characteristic length is often approximated by the secondary dendrite arm spacing (SDAS) in dendritic grains and by the grain size in globular grains.[4] Dendritic grains are, however, generally larger than globular grains. The grain structure observed in the experiments was dendritic with an average grain size of ~ 250 and ~ 350 μm.[28] The characteristic length value (75 μm) used to describe the permeability of the simulated dendritic grains is a reasonable approximation of the actual SDAS, which was not given. Also, the same value can be applied to model globular grains, as they are smaller than dendritic grains.

The size distribution for TiB$_2$ inoculant particles is taken from Reference 38 for 2 kg/ton of grain refiner of type Al-Ti-B and is shown in Figure 3(b). The distribution of inoculant particle population density against undercooling is plotted. The distribution is discretized into 20 classes ($m = 20$).

The transport equations are solved with a Finite Volume Method (FVM) and the SIMPLE algorithm for staggered grid is used for pressure-velocity coupling. A SIMPLE algorithm based FVM code has been previously employed by Založnik et al.[39] to simulate
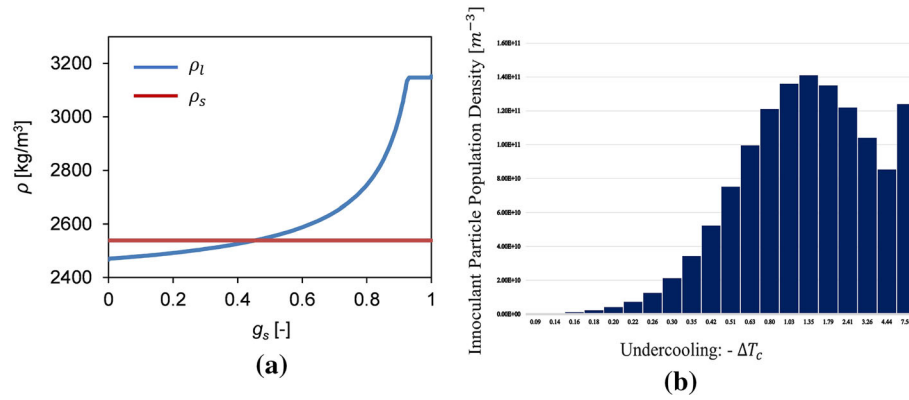
Fig. 3—(*a*) Density as a function of solid fraction using the Scheil model for the solidification path and (*b*) inoculant distribution.

unsteady thermal natural convection in conditions representative of DC casting and has been compared with a highly accurate spectral code. The comparisons showed that a SIMPLE-algorithm based FVM code can be sufficiently accurate to resolve the flow physics. This establishes our confidence in using the SIMPLE algorithm for the current study. The convective terms are discretized with a first-order upwind scheme and for time discretization a fully implicit first-order scheme is used. For all simulations, a structured grid of 8192 cells ($N_r \times N_z = 64 \times 128$) is employed. Submerged boundary conditions are used to account for the fixed disk below the inlet for Inlet 1. The time step (for macroscopic transport) is set constant to 0.03 s, and the simulations are run until steady-state conditions prevail. Each case took around 8 h of CPU time using 8 physical cores in Abel computer cluster. The cluster has compute nodes with 64 GB memory and use the Linux Operating system (64 bit CentOS 6).

V. RESULTS AND DISCUSSION

All studied cases are summarized in Table IV. A total of four cases (1–4) based on the inlet mechanism and grain growth model are considered. Similar to the flow characterization done in Zhang *et al.*,[21,28] a Low Rayleigh number (LRN) turbulent energy-pseudo turbulent dissipation ($k - \varepsilon$) model was used to address the turbulence problem in this simulation. For Case 1 and Case 3, a globular grain morphology is assumed by imposing $g_{\text{env}} = g_s$. For Cases 2 and 4, the grain morphology is simulated, revealing the impact of dendritic growth.

A. *Inlet 1*

Figure 4(a) shows the macrosegregation of Zn together with relative velocity, $\vec{v}_l - \vec{V}_{\text{cast}}$, vectors for Case 1. The macrosegregation patterns of Mg and Cu closely follow that of Zn and are not plotted in this study. Such similarity was also observed in the experimental observations. For the sake of simplicity, we omit the averaging notation when describing the

Table IV. Simulation Cases

Description	Case
Inlet 1—Globular Grain Growth Model	1
Inlet 1—Dendritic Grain Growth Model	2
Inlet 2—Globular Grain Growth Model	3
Inlet 2—Dendritic Grain Growth Model	4

volume-averaged solid and liquid velocities ($\vec{v}_l^1 = \vec{v}_l$ and $\vec{v}_s^s = \vec{v}_s$) from now on. The impact of forced convection due to the fixed disk is restricted close to the surface, as can be seen from the direction of relative velocity vectors. Close to the surface the cooling rate is high, which results in rapid grain growth and only a narrow region of slurry regime ($0 < g_s < g_{\text{pack}}$) is observed. Thus, the contribution from grain motion is less significant close to the surface, and the macrosegregation formation is primarily from the natural and forced convections (liquid flow through packed solid phase) and shrinkage-induced flow that acts in the packed regime (indicated by arrows perpendicular to solid fraction contours). The cooling rate decays toward the center of the billes, and the size of the slurry region grows. Grain transport significantly affects the shape of the sump and the evolution of the solid fraction toward the center of the billet. Since the solid density is higher than liquid density up to a solid fraction 0.5 (Figure 3(a)), grains tend to settle at the center of the billet resulting in negative segregation. The settling of the grains results in expulsion of liquid in the upward direction which can be seen in Figure 4(c). Shrinkage-induced flow also acts in this region but is significant only in the packed regime, where it contributes to the negative segregation. The overall macrosegregation profile, shown in Figure 6(a) for Case 1, has negative segregation at the center of the billet and slightly positive segregation toward the surface. Comparing the radial profile of Case 1 to the experimental profile shows an overprediction of negative segregation in the center of the billet and underprediction of the subsurface and surface segregations.
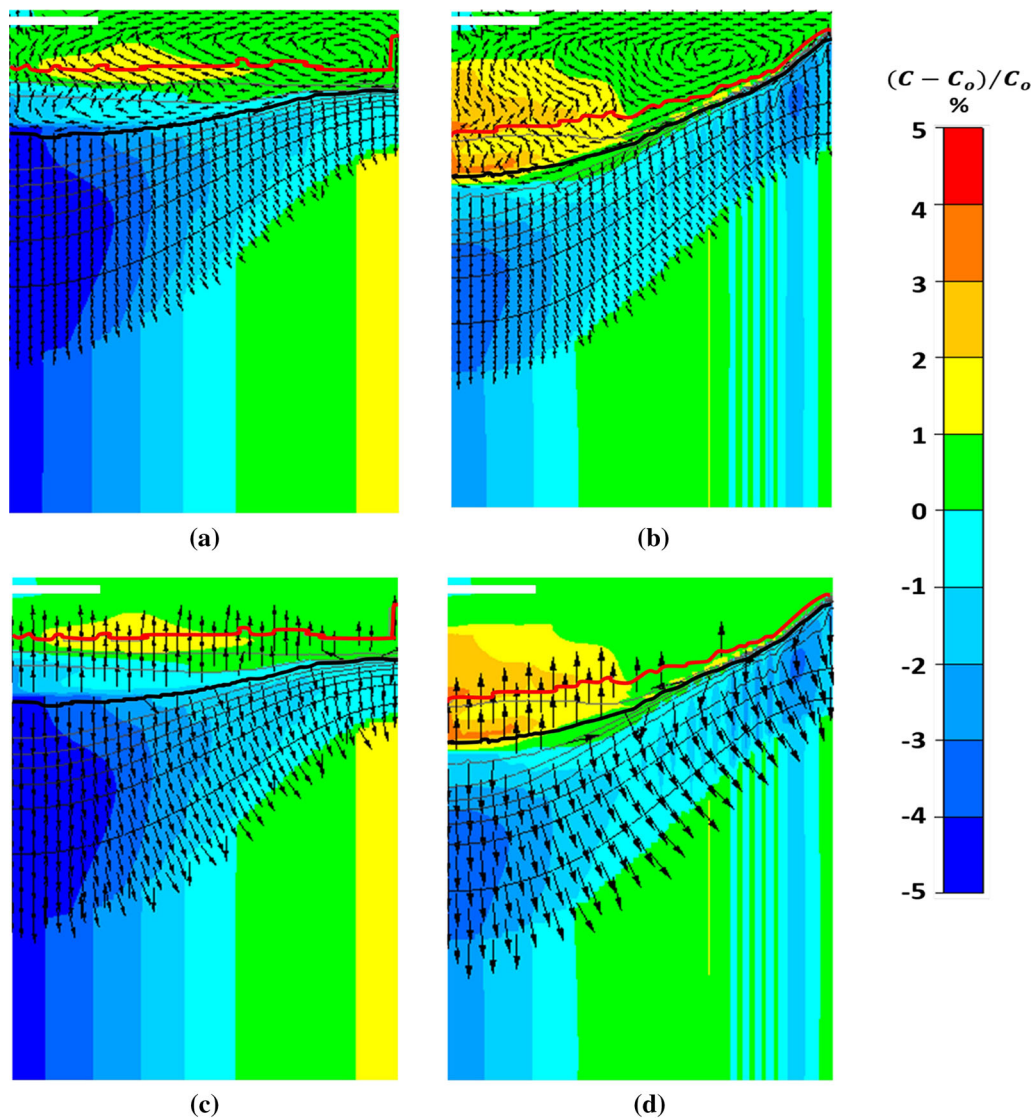
Fig. 4—(a) and (b) Relative composition of Zn in pct together with relative velocity $\vec{v}_l - \vec{V}_{cast}$ vectors and iso-lines of solid fraction for Case 1 and envelope fraction for Case 2; (c) and (d) relative composition of Zn in pct together with relative velocity $\vec{v}_l - \vec{v}_s$ vectors and iso-lines of solid fraction for Case 1 and envelope fraction for Case 2. Only the right half of the cross-section of the billet is shown with the left vertical edge which corresponds to the symmetric axis. The liquidus and the packing front are marked by thick red and black curves. (e) The common color bar of relative segregation for all cases (Color figure online).

For Case 2, we introduce the dendritic model. As the evolution of the envelope fraction differs from the solid fraction, grain packing occurs at lower solid fractions for more pronounced dendritic morphology. The radial profile of internal solid fraction ($g_{intern} = g_s/g_{env}$) at packing is plotted in Figure 7(a) for Case 2. Globular morphology is indicated by internal solid fractions close to 1, whereas dendritic morphology is indicated by internal solid fractions close to 0. Due to the increased cooling rate and local undercooling, the grains become more dendritic close to the cooled surface. As we move toward the center of the billet, the cooling rate decays, but grain transport also has a strong impact on the cooling rate experienced by the free-floating growing grains. The cooling rate of an individual free-floating equiaxed grain depends on the trajectory it makes through the mushy zone. Many of the grains found in

the billet center went through slow cooling not only because the distance between the liquidus and solidus in the center is larger, but primarily because they traveled a long distance through a very weakly undercooled slurry zone before settling to their final location. Their growth was thus even slower than that indicated by the estimation given by the mushy zone thickness. As a result, the grains are more globular in the billet center. This feature is well reproduced by the radial profile in Figure 7(a). The impact of the grain motion on the grain growth is shown in Figure 8(a). The map of constitutional undercooling in the solidification zone clearly shows that nucleation occurs only in a very limited region adjacent to the packing front in the outer half of the billet. Grains found in the billet center are thus also generated in the nucleation region and pass through a prolonged stage of slow growth on their trajectory to the
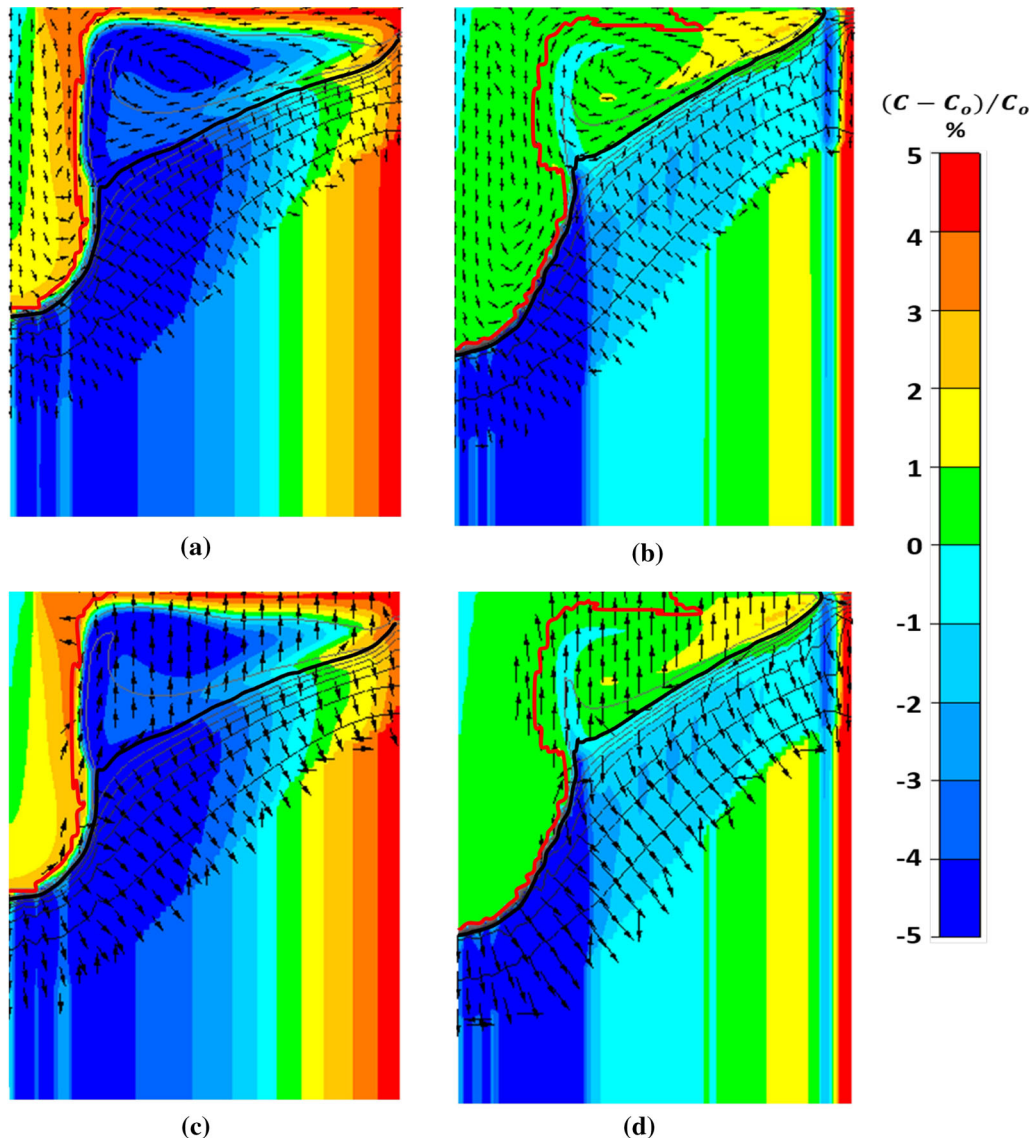
Fig. 5—(a) and (b) Relative compositions of Zn in pct together with relative velocity $\vec{v}_l - \vec{V}_{cast}$ vectors and iso-lines of solid fraction for Case 3 and envelope fraction for Case 4; (c) and (d) relative compositions of Zn in pct together with relative velocity $\vec{v}_l - \vec{v}_s$ vectors and iso-lines of solid fraction for Case 3 and envelope fraction for Case 4. Only the right half of the cross-section of the billet is shown with the left vertical edge which corresponds to the symmetric axis. The liquidus and the packing front are marked by thick red and black curves, respectively. (e) The common color bar of relative segregation for all cases (Color figure online).

final position. We can also observe that the maximum in the experimental profile of grain size (at around 100 mm from the centerline), shown in Figure 6(c), coincides with the point of detachment of the flow from the packing front. It is probable that the peak in grain size appears here because there is no grain nucleation and there is only weak grain settling at this location. Close to the surface, only a narrow region of grain motion is observed as the grains pack at a low solid fraction, and the permeability is sufficiently high to allow a significant liquid velocity through the packed region. This can be seen in Figure 4(b). Consequently, the macrosegregation close to the surface is primarily formed by forced convection and by thermosolutal natural convection through the packed grain layer, resulting in negative

segregation close to the surface and in positive segregation toward mid-radius. Toward the center of the billet, the grains become less dendritic, and grain transport becomes an important mechanism of macrosegregation. Similar to globular grains in the previous case, the coarsely dendritic grains settle at the center of the billet. This results in expulsion of solute-rich liquid indicated by the upward arrows in Figure 4(d). Since dendritic grains pack at lower solid fractions, the intensity of solute depletion is less severe compared with Case 1, where the grains were fully globular. Finally, the shrinkage-induced flow acts in similar fashion as in Case 1, producing negative segregation at the center and positive segregation toward the surface.
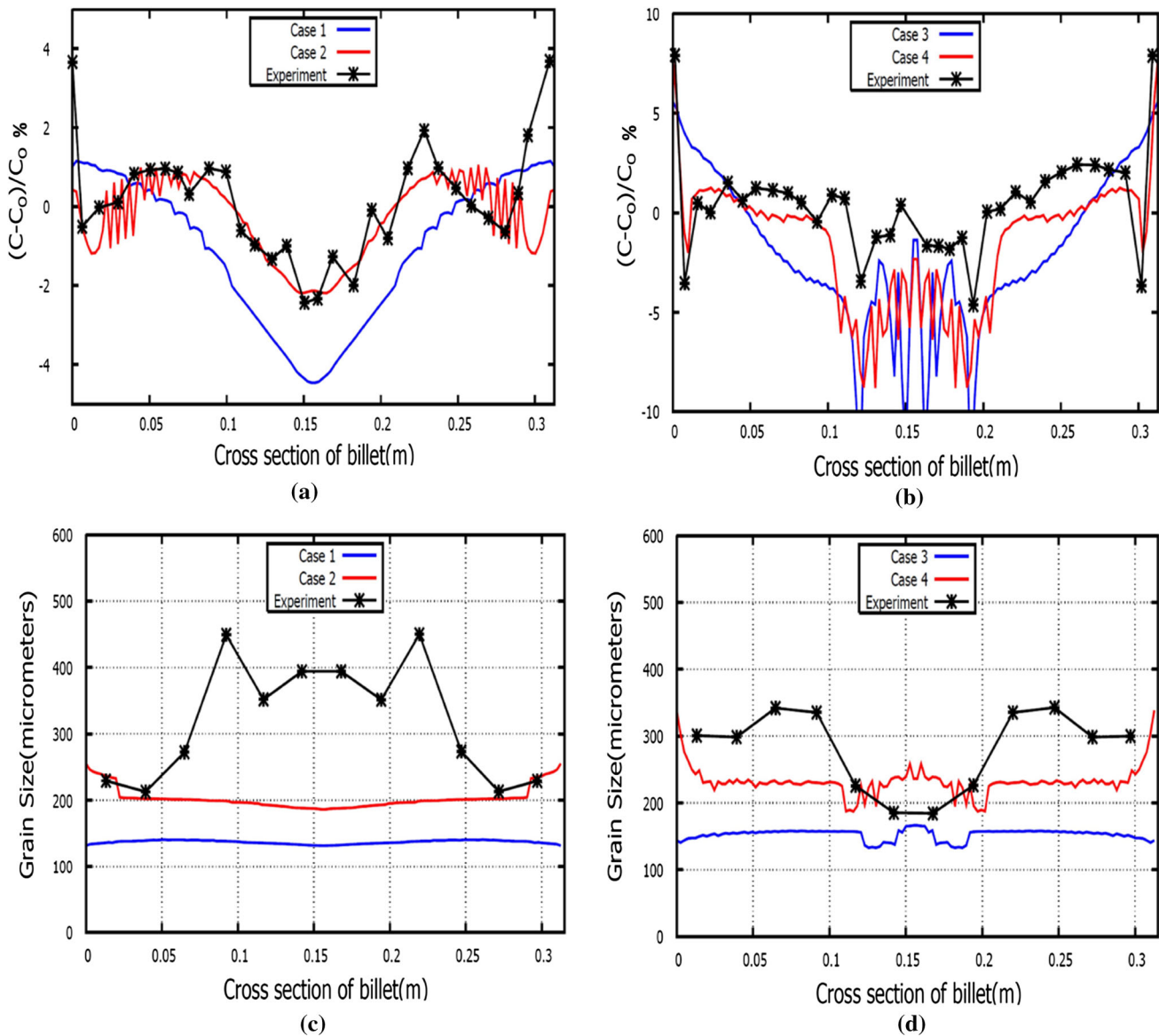
Fig. 6—(*a*) Radial profiles of macrosegregation in Zn from simulation shown for Case 1 and Case 2; (*b*) radial profiles of macrosegregation in Zn from simulation shown for Case 3 and Case 4; (*c*) radial profiles of grain size from simulation shown for Case 1 and Case 2; (*d*) radial profiles of grain size from simulation shown for Case 3 and Case 4. Experimental profile shown in black for both macrosegregation and grain size.

The grain morphology given by the dendritic model clearly indicates a tendency toward globularization or dendritization of the local equiaxed microstructure, but is not to be considered as quantitatively predictive. The predictions depend somewhat on the choice of assumptions and constitutive models, the envelope shape and the primary tip growth kinetics having the largest impact. The present model assumes a spherical envelope shape and hemispherical dendrite tips. Different pertinent models have been used in literature: envelopes of spherical,[30,40–42] octahedral[4,11,12,41,43] and hexapod[12] shape, and dendrite tip growth laws based on hemispherical and paraboloidal tips. In general, spherical envelopes lead to smaller specific envelope surface area per grain volume and to larger fractions of intergranular liquid.[11] As shown in several studies,[11,41,44,45] spherical envelopes lead to predictions of somewhat smaller internal solid fraction than octahedral envelopes. This is mainly due to the larger volume of the envelopes, while the volume of the solid phase remains very similar. The stronger assumption is that of hemispherical tips. At the same undercooling, hemispherical tips grow significantly faster than paraboloidal tips. Detailed analyses have shown that at given solidification conditions the hemispherical tip model predicts a more dendritic grain morphology than the paraboloidal tip model.[4,41,45] While a similar globular-dendritic transition is predicted with both models, the transition from dendritic to globular is shifted to higher grain densities or lower cooling rates with the hemispherical tip model.
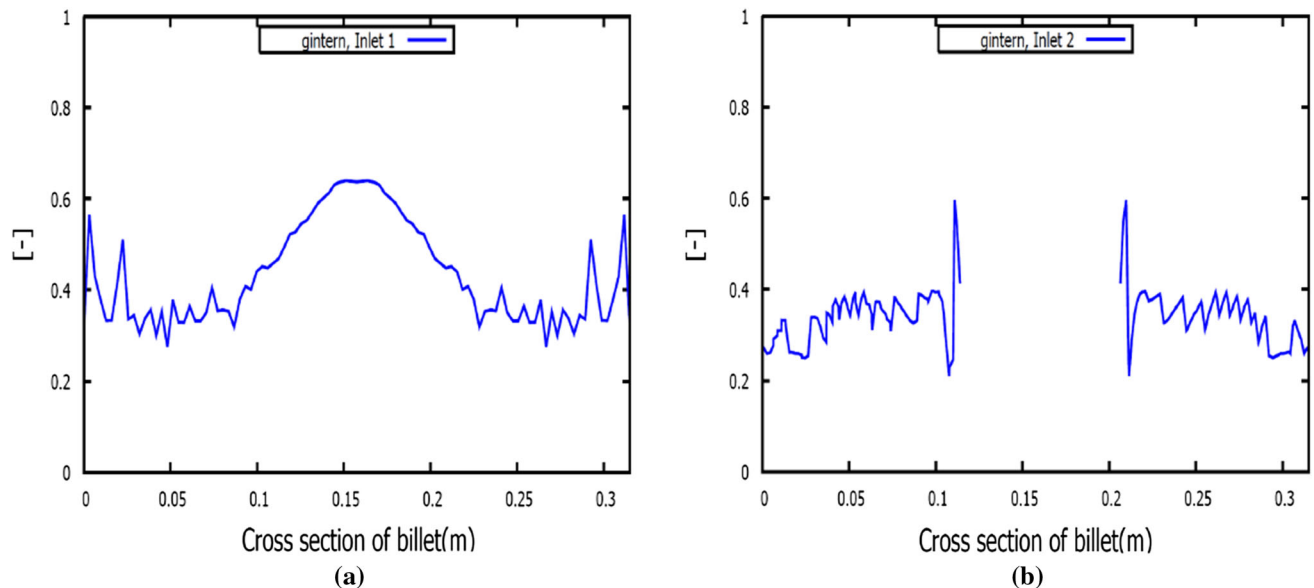
Fig. 7—Radial profiles of internal solid fraction (g_{intern}) at the instant of packing for (*a*) Case 2 and (*b*) Case 4.

For example, Nielsen *et al.*[41] argued that the spherical envelope and the hemispherical tip models gave better predictions of the experimentally observed morphologies of interacting grains in inoculated Al-Cu alloys than the paraboloidal tip model and octahedral envelopes. The physical reasons for this were not explained, but it is clear that dendrite growth models based on models of free dendritic growth are rather simplistic for describing the growth of the strongly interacting grains, and that improved constitutive models are needed.[46]

The final macrosegregation profile for Case 2 is shown in Figure 6(a) along with Case 1 and with the experimental profile. The intensity of the centerline negative segregation and of the mid-section positive segregation are both very well reproduced by Case 2 when compared with the experiment. The surface and subsurface segregations are only qualitatively reproduced. The surface region is strongly influenced by forced convection, and this could be the main source of error. In the current simulation, the semi-horizontal melt feeding scheme used in the experiments is simplified by an inlet-distributor setup. This might not accurately reproduce the flow pattern, which can affect the macrosegregation formation close to the surface. Figure 6(c) compares the grain sizes for Case 1 and 2 to the experimentally measured grain size. On the experimental profile, the grains are smallest close to the surface where the cooling rate is high. Grains coarsen toward the center of the billet due to the decayed cooling rate. These variations are not predicted by the numerical model, which predicts rather flat profiles. The grain size predicted by Case 2 in the vicinity of the billet surface compares well with experimental data.

B. *Inlet 2*

Figure 5(a) shows the macrosegregation pattern of Zn together with the relative velocity $\vec{v}_l - \vec{V}_{cast}$ vectors for Case 3. Compared to the flow pattern observed for Inlet 1, the flow pattern seen for Inlet 2 is completely different due to the vertical jet in the center of the billet. Two flow loops can be seen—a counter clockwise loop in the central area and a clockwise loop between the quarter-radius and the surface of the billet. They collide around 40 mm from the center of the billet. The resulting solid fraction profile shows a cliff shaped pattern (almost vertical solidification front) in this region. Similar flow pattern and solidification front are seen in the simulated profiles using ALSIM6 in Reference 28.

In the center of the billet, macrosegregation formation is mainly caused by washing of the solute due to the strong upstream flow resulting from the forced convection. This can cause severe depletion near the cliff shaped region. An additonal cause of negative segregation is the stacking up of globular grains that are formed next to the cliff or are formed earlier at other locations and are carried to the cliff by the melt flow. The collision of two flow loops around this vertical solidification front blocks the horizontal movement of the solid grains. Hence, the suspension of grains and the washing away of solute due to forced convection result in severe solute depletion of this region. In addition, shrinkage-induced flow also contributes to the negative segregation. The segregation profile can be seen in Figure 6(b). In the mid-section, we can observe some depletion. The forced convection is not strong in this area and the major contribution to macrosegregation is grain settling, which is indicated by the relative velocity vectors between liquid and solid (upward vectors) shown in Figure 5(c). Toward the surface we can see positive segregation, which can be explained as a consequence of grain settling in the mid-radius region. As grains settle in the mid-radius region, the stratified solute is caught up in the clockwise flow loop and gets deposited close to the surface, resulting in positive segregation.
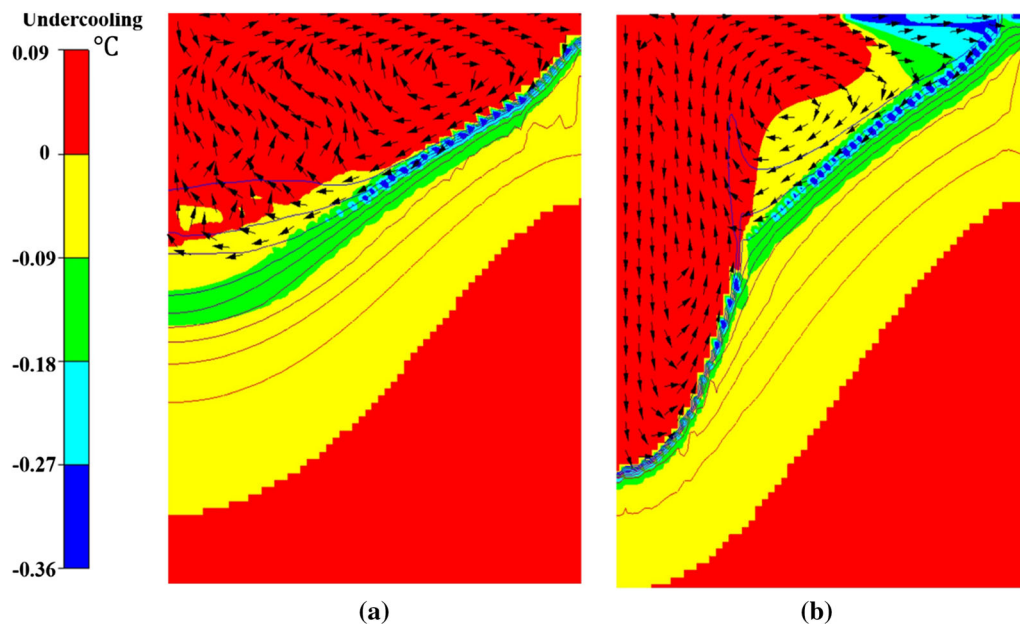
Fig. 8—Undercooling in the billet for (*a*) Case 2 and (*b*) Case 4, indicating regions of nucleation (blue and green), grain growth (yellow), and grain remelting (red). The solid velocity vectors (black) show the grain trajectories through the solidification zone. The lines are isopleths of envelope fraction (Color figure online).

Shrinkage-induced flow additionally contributes to positive segregation in this region. The comparison with the experimental profile shows that for Case 3 (Figure 6(b)), there is an over prediction of negative segregation in the center and inaccurate prediction of macrosegregation at mid-radius and in the vicinity of the surface.

For Case 4, we employ the dendritic model. The flow pattern for this case, shown in Figure 5(b), is similar to the flow pattern for Case 3, shown in Figure 5(a). The only difference is that the grains are dendritic in Case 4. A measure of dendritic morphology can be seen in Figure 7(b). We could not track the internal solid fraction profile in the center due to limited or non-existent grain motion. Around 40 mm away from the center, some coarse dendritic grains ($g_{intern} \sim 0.6$) were observed. The pileup of dendritic grains along the vertical solidification front is similar to that observed with globular grains in Case 3; however, the intensity of segregation is less severe because the dendritic grains pack at lower solid fractions. Nonetheless, additional depletion of solute occurs in the center due to forced convection and shrinkage-induced flow. At mid-radius grain settling dominates, which can be seen by the upward vectors ($\vec{v}_l - \vec{v}_s$) from Figure 5(d). However, due to the dendritic grain morphology in this region ($g_{intern} \sim 0.3$), the intensity of negative segregation due to grain settling is not severe. The transport of solute-rich liquid ejected in the settling region to the surface by the clockwise flow loop is also weakened. The main contributor for the macrosegregation in subsurface and surface areas is the shrinkage-induced flow, which results in negative and positive segregations, respectively.

Comparison with the experimental macrosegregation profile shows that for Case 4 (Figure 6(b)), there is an over prediction of negative segregation in the center. It should, however, be noted that the depletion of solute in the center is not as intense as in Case 3, where the grains were globular. In the mid-section, the simulated profile from Case 4 qualitatively follows the experimental profile, and a very good match between them can be seen close to the surface. In Case 4, the macrosegregation profile compares reasonably well with the experiment, with some discrepancy in the center. This could possibly be explained by overprediction of negative segregation due to insufficient resolution of turbulence (2 equation model), which could result in excessive washing away of the solute in the center. In Figure 6(d), we compare the experimental profile of grain size with simulated profiles from Cases 3 and 4. In the vertical melt-feeding scheme, intense flow is observed in the center. Due to the particular shape of the solidification front, the cooling rate is quite high in the center. As a result, small grains are observed in the central part of the billet. The grain size increases toward the mid-radius and slightly decreases at the surface. In Case 3, an almost flat profile of grain size is predicted. The correct order of magnitude of the grain size is predicted for Case 4, but the grain size variations across the billet diameter are not correctly reproduced. The coarse grain structure at mid-radius seen in the experiment is not directly predicted by Case 4. A more detailed analysis of grain nucleation, growth, and transport, shown in Figure 8(b), shows that the reported coarse grain region is located at the meeting point of the two flow circulations. Because of the flow orientation the deposition rate of free-floating equiaxed grains at the meeting point is weak. Also, the meeting point is a region of very low undercooling, *i.e.*, without nucleation of new grains. The structure at this location is therefore composed of

few slowly growing grains, resulting in a localized band of coarse grain morphology.

VI. CONCLUSIONS

A simplified three-phase, multiscale solidification model that couples macroscopic transport and equiaxed grain growth was previously proposed.[3] This model was novel in its approach as it introduces three phases in describing equiaxed grain growth but solves only two-phase macroscopic transport equations. A limited demonstration of the model to predict macrosegregation in DC casting accounting for grain morphology was done previously. In this paper, we conducted a proper validation study by both imposing globular morphology and simulating dendritic morphology and comparing with experiments.

Two different types of inlet melt flow were considered. In the first type, the geometry was simplified in the simulation, which resulted in slight variations in macrosegregation prediction toward the surface of the billet compared with experiment. However, the centerline depletion and mid-radius segregation were well predicted when dendritic grain morphology was considered. In the second type of inlet, macrosegregation formation predicted by the numerical model considering dendritic morphology could be qualitatively compared with the experimental data. For both types of inlets, a model using a globular grain morphology overpredicted the negative segregation at the center and led to inaccurate prediction of macrosegregation in other parts of the billet. These results indicate the necessity of accurate modeling of grain morphology.

Grain size predictions give the right order of magnitude compared with experimental observations, especially when dendritic morphology is accounted for. However, the variation of the grain size across the cross-section of the billet is not accurately predicted by the model for both inlet types. Several modeling aspects can affect the grain size and morphology prediction. Packing fraction is one of them and its value is ambiguous. Another aspect is the inaccurate resolution of the nucleation zone. In DC casting process, the nucleation zone is very small, and even reasonably fine grids might not be able to resolve it completely. Therefore, this could be a critical factor. Finally, the current model uses simplified constitutive models to predict grain growth in the presence of important solutal interactions between growing grains. Advanced constitutive models have been proposed recently,[46] which could be integrated into the current model. These are some of the aspects which could be clarified in future study.

NOMENCLATURE

$\langle C_i, \rangle$	Average mass concentration of solute i (wt pct)
$\langle C_i^* \rangle$	Average equilibrium mass concentration of solute i (wt pct)
$C_{o,i}$	Mean concentration of solute i (wt pct)
c_p	Specific heat (J kg^{-1} K)
C_D	Drag co-efficient (–)
d	Diameter of inoculant particle (m)
$D_{,i}$	Diffusion coefficient of solute i (m^2 s^{-1})
g	Volume fraction (–)
g_{pack}	Packing fraction (–)
g_{intern}	Internal solid fraction (–)
$\vec{g}$	Acceleration due to gravity (m s^{-2})
$\langle h_l \rangle^1$	Averaged liquid enthalpy (J kg^{-1})
$\langle h_s \rangle^s$	Averaged solid enthalpy (J kg^{-1})
h_m	Mixture enthalpy (J kg^{-1})
$h_{primary}$	Primary cooling heat-transfer coefficient (W m^{-2} K^{-1})
$h_{secondary}$	Secondary cooling heat-transfer coefficient (Wm^{-2} K^{-1})
$k_{p,i}$	Partition coefficient of solute i (–)
K	Permeability (m^2)
L_f	Latent heat of fusion (J kg^{-1})
l_{kc}	Characteristic length for permeability (m)
$m_{l,i}$	Liquidus slope of solute i, K (wt pct^{-1})
N_{nuc}^i	Volumetric number density (m^{-3})
N_g	Grain density (m^{-3})
p_l	Liquid pressure (N m^{-2})
P	Perimeter of the ingot (m)
Q_{water}	Water flow rate (m^3 s^{-1})
R_{env}	Radius of the envelope (m)
$R^{s,eq}$	Radius of the solid grain (m)
Re	Reynolds number
S_v	Interfacial area density (m^{-1})
Sc	Schmidts number
t	Time (s)
T	Temperature (K)
T_{water}	Temperature of cooling water (K)
T_{sat}	Temperature of boiling water (K)
T_{cast}	Casting temperature (K)
T_{liq}	Temperature of liquidus (K)
T_m	Melting temperature of pure Al (K)
T_{eut}	Eutectic temperature (K)
ΔT	Undercooling (K)
ΔT_c	Critical undercooling for nucleation (K)
$\langle \vec{v}_l \rangle^1$	Intrinsic average velocity of liquid phase (ms^{-1})

$\langle \vec{v}_s \rangle^s$	Intrinsic average velocity of solid phase (ms^{-1})
$\vec{V}_{\mathrm{cast}}$	Casting velocity (ms^{-1})
V_{tip}	Velocity of dendrite tip (ms^{-1})
β_T	Thermal expansion coefficient (K)
$\beta_{C,i}$	Solutal expansion coefficient of solute i, $(\mathrm{pct\ w}^{-1})$
δ_i	Diffusion length of solute $i\ (-\ \mathrm{m})$
$\delta(t)$	Dirac function
Γ_{GT}	GIBBS–Thomson co-efficient (Km)
Γ	Growth rate $(\mathrm{kg\ m}^{-3}\ \mathrm{s}^{-1})$
κ	Thermal conductivity $(\mathrm{W\ m}^{-1}\ \mathrm{K})$
ρ_l	Liquid density $(\mathrm{kg\ m}^{-3})$
ρ_s	Solid density used to account for shrinkage $(\mathrm{kg\ m}^{-3})$
$\rho_{l,b}$	Liquid buoyancy density used to account for Bousinessq approximation $(\mathrm{kg\ m}^{-3})$
$\rho_{s,b}$	Solid buoyancy density used to account for grain motion $(\mathrm{kg\ m}^{-3})$
ρ_m	Mixture density $(\mathrm{kg\ m}^{-3})$
μ_l	Liquid dynamic viscosity (Pa s)

SUBSCRIPTS AND SUPERSCRIPTS

l	Liquid
s	Solid
env	Envelope
e	Extragranular liquid
d	Intragranular liquid
s–d	Solid–liquid interface
e–d	Intra-extra granular liquid interface
*	equilibrium
l,b	Liquid buoyancy
s,b	Solid buoyancy

REFERENCES

1. A.V. Reddy and N.C. Beckermann: *Metall. Mater. Trans. B*, 1997, vol. 28B, pp. 479–89.
2. G. Lesoult, V. Albert, B. Appolaire, H. Combeau, D. Daloz, A. Joly, C. Stomp, G.U. Grün, and P. Jarry: *Sci. Technol. Adv. Mater.*, 2001, vol. 2, pp. 285–91.
3. K.O. Tveito, A. Pakanati, M. M'Hamdi, H. Combeau, and M. Založnik: *Metall. Mater. Trans. A*, 2018, vol. 49A, pp. 2778–94.
4. L. Heyvaert, M. Bedel, M. Založnik, and H. Combeau: *Metall. Mater. Trans. A*, 2017, vol. 48A, pp. 4713–34.
5. A. Olmedilla, M. Založnik, B. Rouat, and H. Combeau: *Phys. Rev. E*, 2018, https://doi.org/10.1103/physreve.97.012910.
6. M. Bedel, K.O. Tveito, M. Založnik, H. Combeau, and M. M'Hamdi: *Comput. Mater. Sci.*, 2015, vol. 102, pp. 95–109.
7. M. Rappaz: *Int. Mater. Rev.*, 1989, vol. 34, pp. 93–124.
8. J. Ni and C. Beckermann: *Metall. Trans. B*, 1991, vol. 22, pp. 349–61.
9. C.Y. Wang and C. Beckermann: *Metall. Mater. Trans. A*, 1996, vol. 27A, pp. 2754–64.
10. M. Wu, A. Ludwig, A. Buhrig-Polaczek, M. Fehlbier, and P.R. Sahm: *Int. J. Heat Mass Transf.*, 2003, vol. 46, pp. 2819–32.
11. M. Wu and A. Ludwig: *Acta Mater.*, 2009, vol. 57, pp. 5621–31.
12. M. Wu, A. Fjeld, and A. Ludwig: *Comput. Mater. Sci.*, 2010, vol. 50, pp. 43–58.
13. M. Založnik and H. Combeau: *Comput. Mater. Sci.*, 2010, vol. 48, pp. 1–10.
14. H. Combeau, M. Založnik, S. Hans, and P.E. Richy: *Metall. Mater. Trans. B*, 2009, vol. 40B, pp. 289–304.
15. A. Kumar, M. Založnik, and H. Combeau: *Int. J. Adv. Eng. Sci. Appl. Math.*, 2010, vol. 2, pp. 140–48.
16. J. Li, M. Wu, A. Ludwig, and A. Kharicha: *Int. J. Heat Mass Transf.*, 2014, vol. 72, pp. 668–79.
17. M. Wu, A. Ludwig, and A. Kharicha: *Steel Res. Int.*, 2018, vol. 89, pp. 1–14.
18. T. Jalanti: PhD thesis, Ecole Polytechnique Fédérale de Lausanne, Laussanne, Switzerland, 2000.
19. C.J. Vreeman and F.P. Incropera: *Int. J. Heat Mass Transf.*, 2000, vol. 43, pp. 687–704.
20. M. Založnik and B. Šarler: *Model. Cast. Weld. Adv. Solidif. Process. XI*, 2006, pp. 243–50.
21. L. Zhang, D.G. Eskin, A. Miroux, T. Subroto, and L. Katgerman: *IOP Conf. Ser. Mater. Sci. Eng.*, 2012, vol. 33, pp. 1–8.
22. Q. Du, D.G. Eskin, and L. Katgerman: *Metall. Mater. Trans. A Phys. Metall. Mater. Sci.*, 2007, vol. 38, pp. 180–89.
23. A.V. Reddy and C. Beckermann: *Mater. Process. Comput. Age*, 1995, vol. 2, pp. 89–102.
24. M. Založnik, A. Kumar, H. Combeau, M. Bedel, P. Jarry, and E. Waz: *Adv. Eng. Mater.*, 2011, vol. 13, pp. 570–80.
25. A. Hakonsen, D. Mortensen, S. Benum, and H.E. Vatne: *Light Metals*, TMS, Warrendale, PA, 1999, pp. 821–27.
26. M. Bedel, L. Heyvaert, M. Založnik, H. Combeau, D. Daloz, and G. Lesoult: *IOP Conf. Ser. Mater. Sci. Eng.*, 2015, vol. 84 (1), pp. 1–8.
27. H. Combeau, M. Založnik, and M. Bedel: *JOM*, 2016, vol. 68, pp. 2198–2206.
28. L. Zhang, D.G. Eskin, A. Miroux, T. Subroto, and L. Katgerman: *Metall. Mater. Trans. B*, 2012, vol. 43B, pp. 1–9.
29. A.L. Greer, A.M. Bunn, A. Tronche, P.V. Evans, and D.J. Bristow: *Acta Mater.*, 2000, vol. 48, pp. 2823–35.
30. M. Rappaz and P.H. Thévoz: *Acta Metall.*, 1987, vol. 35, pp. 2929–33.
31. M. Rappaz and W.J. Boettinger: *Acta Mater.*, 1999, vol. 47, pp. 3205–19.
32. D. Weckman and P. Niessen: *Metall. Trans. B*, 1982, vol. 13, pp. 593–602.
33. A.L. Dons, E.K. Jensen, Y. Langsrud, E. Trømborg, and S. Brusethaug: *Metall. Mater. Trans. A*, 1999, vol. 30A, pp. 2135–46.
34. Y. Du, Y.A. Chang, B. Huang, W. Gong, Z. Jin, H. Xu, Z. Yuan, Y. Liu, Y. He, and F.Y. Xie: *Mater. Sci. Eng. A*, 2003, vol. 363, pp. 140–51.
35. C.J. Vreeman, M.J.M. Krane, and F.P. Incropera: *Int. J. Heat Mass Transf.*, 2000, vol. 43, pp. 677–86.
36. I. Vušanović and M.J.M. Krane: *Mater. Sci. Eng.*, 2011, vol. 1, pp. 1–12, https://doi.org/10.1088/1757-899x/27/1/012069.
37. A. Pakanati, K.O. Tveito, M. M'Hamdi, H. Combeau, and M. Založnik: in *Light Metals 2018. TMS 2018*. The Minerals, Metals & Materials Series, Martin O. ed., Springer, Cham, 2018, pp. 1089–96.
38. A. Tronche: PhD thesis, University of Cambridge, Cambridge, England, 2000.
39. M. Založnik, S. Xin, and B. Šarler: *Int. J. Numer. Methods Heat Fluid Flow*, 2008, vol. 18, pp. 308–24.
40. C.Y. Wang and C. Beckermann: *Metall. Trans. A*, 1993, vol. 24, pp. 2787–2802.
41. Ø. Nielsen, B. Appolaire, H. Combeau, and A. Mo: *Metall. Mater. Trans. A*, 2001, vol. 32A, pp. 2049–60.
42. M.A. Martorano, C. Beckermann, and C.A. Gandin: *Metall. Mater. Trans. A*, 2003, vol. 32A, pp. 1657–74.
43. B. Appolaire, H. Combeau, and G. Lesoult: *Mater. Sci. Eng. A*, 2008, vol. 487, pp. 33–45.
44. M. Wu and A. Ludwig: *Acta Mater.*, 2009, vol. 57, pp. 5632–44.
45. M. Bedel: PhD theses, Université de Lorraine, Nancy, France, 2014.
46. M. Torabi Rad, M. Založnik, H. Combeau, and C. Beckermann: *Materialia*, 2019, article in press.